

Towards a two-scale model for morphogenesis - How cellular processes influence tissue deformations

Lea Happel¹ and Axel Voigt^{1,2,3*}

¹Institute of Scientific Computing, TU Dresden, 01062, Dresden
Germany.

²Center of Systems Biology Dresden (CSBD), Pfotenhauerstr. 108,
01307, Dresden Germany.

³Cluster of Excellence, Physics of Life (PoL), TU Dresden, Arnoldstr.
18, 01307, Dresden Germany.

*Corresponding author(s). E-mail(s): axel.voigt@tu-dresden.de;
Contributing authors: lea.happel@tu-dresden.de;

Abstract

We propose a two-scale model to resolve essential features of developmental tissue deformations. The model couples individual cellular behavior to the mechanics at tissue scale. This is realized by a multiphase-field model addressing the motility, deformability and interaction of cells on an evolving surface. The surface evolution is due to bending elasticity, with bending properties influenced by the topology of the cellular network, which forms the surface. We discuss and motivate model assumptions, propose a numerical scheme, which essentially scales with the number of cells, and explore computationally the effect of the two-scale coupling on the global shape evolution. The approach provides a step towards more quantitative modeling of morphogenetic processes.

1 Introduction

More than 100 years ago D'Arcy Thompson [1] pointed out correlations between biological forms and mechanical phenomena and postulated that biological shape diversity is revealing of the physical forces driving it. While this postulation today is confirmed, the details of the multiscale process of developmental tissue deformations, which couples individual cellular behavior to the mechanics at tissue scale are

still largely unknown. Indeed, developmental tissue deformations require mechanical forces and during early multicellular development, these forces are often generated in effectively two-dimensional tissues [2]. The large-scale motion during these processes emerges from collective tissue-mechanical properties of multicellular structures. For this reason various continuous theories have been proposed which consider coarse-grained material features and model shape evolution using physical conservation laws, e.g., hydrodynamic theories of active thin shells [3–6], active polar or nematic surfaces [7–11] or models for active fluid deformable surfaces [12–15]. While huge progress has been made with respect to model derivation and numerical simulations [4, 9, 15–18], so far, these models are still unable to quantitatively predict the dynamics of morphogenetic processes. A possible step towards more quantitative modeling is to take processes on the cellular scale stronger into account. Various "discrete" models exist which focus on the cellular scale, e.g., [19–22]. We propose a two-scale coupling mechanism, which intervenes the cellular and the tissue scale. Instead of a continuous theory with coarse-grained material properties we resolve the individual cells in the effectively two-dimensional tissue, and consider their deformability, their motility and their interaction with neighboring cells. These cellular processes form the tissue and determine the mechanical forces required for tissue deformation. However, the coupling is in both directions, the shape of the two-dimensional tissue also influences the cells. In order to account for these couplings we adapt mechanical phenomena known for thin crystalline sheets. Out of plane deformations at topological defects [23–25] is one example. Also in tissues topological defects can be defined. Various efforts relate to orientational defects [26–31]. However, also positional defects play a role. Presumably regions with cells with five or seven neighbors have different mechanical properties than those with cells with only six neighbors. Higher-order vertices or multicellular rosettes also have been shown to have an effect on the mechanics of the tissue [32]. Such defects greatly influence the rigidity of the epithelial tissue. Neighbor exchanges between the cells determine the flow of the tissue and are essential in many important aspects of morphogenesis. The two-scale coupling thus essentially allows to study the influence of cellular processes on the tissue scale. This in principle would also allow to consider genetic and mechano-chemical processes, however, we here refrain from such attempts and only model the cells as deformable active Brownian particles, neglecting any sub-cellular properties. We consider a multiphase-field model to resolve each individual cell, which has been shown to provide a reliable modeling approach, at least in flat space [33–36], next to, e.g., vertex models [32, 37, 38], which operate on the same spatial scales. However we consider this model on an evolving surface, with the evolution defined by the two-dimensional tissue. We therefore extend previous approaches of multiphase-field models on stationary surfaces [39, 40] and combine them with Canham/Helfrich models to consider the bending properties of the tissue.

The outline of the paper is as follows: In Section 2 we introduce the mathematical model, motivate and justify all assumptions, introduce notation and the system of equations and explain how they are discretised. In Section 3 we discuss results, starting from known phenomena of classical continuous models and comparisons with previous studies for cells on stationary geometries, before the full two-scale coupling is fully explored. Finally we discuss the results and draw conclusions in Section 4.

2 Mathematical model

2.1 General description and model assumptions

We make the following assumptions: The thickness of the monolayer of epithelial tissue is assumed to be constant and small compared to its lateral extension. This allows to neglect the thickness and to model the tissue as a two-dimensional surface. We assume this surface to be closed, have constant area, constant enclosed volume and have properties of an elastic film, which can be solid or fluid like, depending on the properties of the tissue. We assume the film to only resist bending and consider a Canham/Helfrich energy. Minimizing this energy under the mentioned constraints using a L^2 -gradient flow essentially determines the shape change and with it the movement of the surface in normal direction. So far we have a fully continuous description of the epithelial tissue. This description is well known from models of fluid membranes. In this context the microscopic constituents, the lipids, are only considered in a coarse-grained manner. Their properties in tangential direction are either considered implicitly [41, 42] or more recently if membrane viscosity is taken into account also explicitly [12, 43–45]. However, also these models are continuous and operate on the same length scale as the Canham/Helfrich energy. In the context of epithelial tissue the surface consists of interacting cells. A coarse-grained description of such a material is a challenging task even in flat space [46–49] and most studies therefore resolve each individual cell. Thereby each cell is modeled as an active deformable object. We consider each cell to have constant area, therefore neglect cell growth or shrinkage, and consider a line tension to energetically evolve its shape. Activity is introduced via a convective term. This, relatively simple description of a cell, can be seen as a generalization of an active Brownian particle [35], and is successfully used to model collective motion in flat space [36, 50] and on curved surfaces [39, 40]. In our context the cell builds part of the surface and a confluent collection of cells, with cell-cell interactions, forms the surface. The constant area of cells thus leads to the constraint of a constant area of the surface. We further assume all cells to have equal size and properties. Within this setting we have a two-scale model which is continuous with respect to bending and thus movement in normal direction, but "discrete", resolving each individual cell, in tangential direction. From experimental and theoretical studies of monolayers of epithelial tissue in flat space it is well known that topological features resulting from the cell arrangements have strong implications on the mechanical properties of the tissue [32, 51]. We here consider a computationally accessible topological feature, the number of neighbors of a cell, to account for this dependency. In order to couple the "discrete" cellular scale to the continuous scale of the surface we make the bending rigidity to depend on the number of neighbors. As for two-dimensional crystalline materials, which buckle at defects [23–25], the bending rigidity is reduced for cells for which the number of neighbors deviate from six, where six corresponds to the optimal hexagonal packing in flat space. This provides additional coupling between the different scales of the two-scale problem. The coupling is in both directions, the cellular arrangement influences the bending rigidity and thus the shape change of the continuous surface and the surface evolution influences the shape and movement of each cell, as the cells are confined to the surface. These couplings allow to explore how activity, which is induced

on the "discrete" cellular scale, lead to morphological changes of the surface on the continuous scale.

2.2 Notation

The considered two-scale model requires basic notation from differential geometry and geometric partial differential equations. We follow the same notation as in [52]. The basic parts are repeated for convenience. We consider a time dependent smooth and oriented surface $\Gamma = \Gamma(t)$ without boundary, embedded in \mathbb{R}^3 and given by a parametrization \mathbf{X} . The enclosed volume is denoted by $\Omega = \Omega(t)$. We denote by \mathbf{n} the outward pointing surface normal, the shape operator is $\mathcal{B} = -\nabla_{\mathbf{P}}\mathbf{n}$ with $\nabla_{\mathbf{P}}$ the tangential derivative, and the mean curvature is $H = \text{tr}\mathcal{B}$. With this notation the mean curvature of the unit sphere is $H = -2$. We further consider the covariant derivative ∇_{Γ} and the covariant divergence $\nabla_{\Gamma}\cdot$, with $\Delta_{\Gamma} = \nabla_{\Gamma}\cdot\nabla_{\Gamma}$ the Laplace-Beltrami operator. Δ_C denotes a componentwise application of Δ_{Γ} . The model in the following should be considered in dimensionless form.

2.3 Model formulation

The simplest mechanical model for a two-dimensional surface that only resists bending is the Canham/Helfrich model which is based on the energy

$$\mathcal{F}_{Helf} = \int_{\Gamma(t)} \frac{1}{2} \kappa_{bending} H^2 d\Gamma(t) \quad (1)$$

where $\kappa_{bending}$ is the bending rigidity and the spontaneous curvature is set to zero [41, 42]. With constraints on constant area and constant enclosed volume the corresponding evolution equations read

$$v_{\mathbf{n}} = -\frac{\delta\mathcal{F}_{Helf}}{\delta\mathbf{X}} \cdot \mathbf{n} - \lambda_{vol} + \lambda_{area} H \quad (2)$$

$$-\lambda_{area} \int_{\Gamma(t)} v_{\mathbf{n}} H d\Gamma(t) = \int_{\Gamma(0)} 1 d\Gamma(0) - \int_{\Gamma(t)} 1 d\Gamma(t) \quad (3)$$

$$\lambda_{vol} \int_{\Gamma(t)} v_{\mathbf{n}} d\Gamma(t) = \frac{1}{3} \int_{\Gamma(0)} \langle \mathbf{X}, \mathbf{n} \rangle d\Gamma(0) - \frac{1}{3} \int_{\Gamma(t)} \langle \mathbf{X}, \mathbf{n} \rangle d\Gamma(t) \quad (4)$$

where $v_{\mathbf{n}}$ is the magnitude of the velocity of the surface in normal direction, λ_{vol} and λ_{area} are Lagrange multipliers (ensuring conservation of the initial volume and area, similar to the technique used in [53]), and

$$\frac{\delta\mathcal{F}_{Helf}}{\delta\mathbf{X}} = \Delta_{\Gamma}(\kappa_{bending} H) \mathbf{n} - \kappa_{bending} H \left(\|\mathcal{B}\|^2 - \frac{H^2}{2} \right) \mathbf{n}. \quad (5)$$

This classical problem is supplemented by a surface multiphase-field model to account for cell arrangements which form the surface. We consider phase-field variables $\phi_i(\mathbf{x}, t)$, one for each cell, with \mathbf{x} defined on the surface Γ . Values of $\phi_i = 1$ and $\phi_i = -1$

denote the interior and exterior of a cell, respectively. The cell boundary is implicitly defined as the zero-level set of ϕ_i . We consider a surface Cahn-Hilliard-like energy

$$\mathcal{F}_{CH} = \frac{1}{Ca} \sum_{i=1}^N \int_{\Gamma(t)} \frac{1}{G(\phi_i)} \left(\frac{\epsilon}{2} \|\nabla_{\Gamma} \phi_i\|^2 + \frac{1}{\epsilon} W(\phi_i) \right) d\Gamma(t), \quad (6)$$

where N denotes the number of cells, Ca is the capillary number, measuring the deformability of the cells, $G(\phi_i) = \frac{3}{2}|1 - \phi_i^2|$ is a de Gennes factor which helps to keep $-1 \leq \phi_i \leq 1$ [54], $W(\phi_i) = \frac{1}{4}(1 - \phi_i^2)^2$ is a double well potential and ϵ a small parameter determining the width of the diffuse interface. Cell-cell interactions are considered by an interaction energy

$$\mathcal{F}_{Int} = \frac{1}{In} \sum_{i=1}^N \sum_{j \neq i} \int_{\Gamma(t)} a_{rep}(\phi_i + 1)^2(\phi_j + 1)^2 - a_{att}W(\phi_i)W(\phi_j) d\Gamma(t) \quad (7)$$

where In is the strength of interaction and a_{rep} and a_{att} model repulsive and attractive components, respectively. The first term in eq. (7) penalizes overlap of the interior of the cells and the second favors overlap of the diffuse interfaces. The last can best be seen considering the equilibrium condition $\frac{\epsilon}{2} \|\nabla_{\Gamma} \phi_i\|^2 \approx \frac{1}{\epsilon} W(\phi_i)$ resulting from the tanh-profile of ϕ_i , see [55]. The form is well established in flat space and also has already been considered on curved surfaces [40]. Adjusting the parameters a_{rep} and a_{att} allows to construct a short-range interaction potential within the diffuse interface, see Figure 1, demonstrating the consistency with other approaches directly implementing an interaction potential [56, 57].

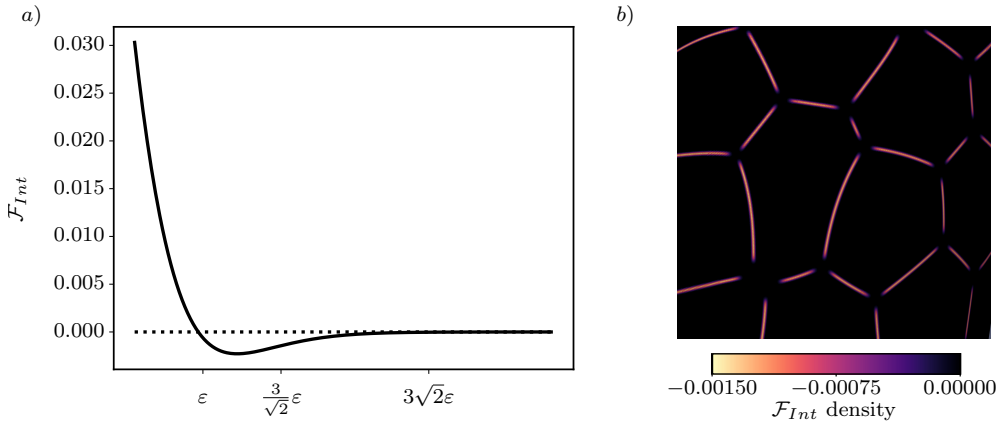


Fig. 1 Short range interaction potential as a function of the distance between the 0-levelsets of two cells a) and in a computational realization highlighting the short range interaction b). The used parameters are $In = 0.05$, $a_{rep} = 0.0625$ and $a_{att} = 0.48$. For a phase-field with the stable phases -1.0 and 1.0 the width of the interface is approximately $3\sqrt{2}\epsilon$ (obtained from the equilibrium tanh-profile). This point is marked explicitly in a). The underlying cell contours for b) can be seen in Figure 2 b).

The evolution equation for each ϕ_i reads

$$\dot{\phi}_i - \phi_i v_{\mathbf{n}} H + v_0 (\mathbf{e}_i \cdot \nabla_{\Gamma} \phi_i) = \Delta_{\Gamma} \frac{\delta(\mathcal{F}_{CH} + \mathcal{F}_{Int})}{\delta \phi_i} \quad (8)$$

which considers conservation of mass and the transport formula

$$\frac{d}{dt} \int_{\Gamma(t)} \phi_i d\Gamma(t) = \int_{\Gamma(t)} \dot{\phi}_i d\Gamma(t) + \int_{\Gamma(t)} \phi_i \nabla_{\Gamma} \cdot (v_{\mathbf{n}} \mathbf{n}) d\Gamma(t),$$

see [58]. Thereby, $\dot{\phi}_i = \partial_t \phi_i + \nabla_{\mathbf{w}} \phi_i$ is the material derivative with $\nabla_{\mathbf{w}} \phi_i = (\nabla_{\Gamma} \phi_i, \mathbf{w})$ and the relative material velocity $\mathbf{w} = v_{\mathbf{n}} \mathbf{n} - \partial_t \mathbf{X}$, see [52, 59], and $-\phi_i v_{\mathbf{n}} H = \phi_i \nabla_{\Gamma} \cdot (v_{\mathbf{n}} \mathbf{n})$. We follow an Lagrangian-Eulerian perspective, Lagrangian in normal direction providing the coupling with the normal velocity $v_{\mathbf{n}}$ and Eulerian in tangential direction. The other terms are as in [39] and contain the self-propulsion strength v_0 and direction $\mathbf{e}_i = (\cos \theta_i, \sin \theta_i)$ considered in a local coordinate system for the tangent plane at the center of mass of cell i . For consistency we define one of the orthonormal vectors of this coordinate system with respect to the projected direction \mathbf{e}_i of the previous time step. The angle θ_i is controlled by rotational noise $d\theta_i(t) = \sqrt{2D_r} dW_i(t)$, with diffusivity D_r and a Wiener process W_i . The variational derivatives read:

$$\frac{\delta \mathcal{F}_{Int}}{\delta \phi_i} = \frac{1}{In} \sum_{j \neq i} \left(4a_{rep}(\phi_i + 1)(\phi_j + 1)^2 - \frac{1}{2} a_{att}(\phi_i(\phi_i^2 - 1))(\phi_j^2 - 1)^2 \right) \quad (9)$$

$$\frac{\delta \mathcal{F}_{CH}}{\delta \phi_i} = \frac{1}{Ca} \left(\frac{1}{G(\phi_i)} \frac{1}{\epsilon} W'(\phi_i) - \frac{\epsilon}{G(\phi_i)} \Delta_{\Gamma} \phi_i + \left(\frac{1}{G(\phi_i)} \right)' \left(\frac{1}{\epsilon} W(\phi_i) - \frac{\epsilon}{2} \|\nabla_{\Gamma} \phi_i\|^2 \right) \right), \quad (10)$$

where the last can be simplified using the equilibrium condition $\frac{\epsilon}{2} \|\nabla_{\Gamma} \phi_i\|^2 \approx \frac{1}{\epsilon} W(\phi_i)$ to obtain the approximation [54]

$$\frac{\delta \mathcal{F}_{CH}}{\delta \phi_i} = \frac{1}{Ca} \left(\frac{1}{G(\phi_i)} \frac{1}{\epsilon} W'(\phi_i) - \frac{\epsilon}{G(\phi_i)} \Delta_{\Gamma} \phi_i \right). \quad (11)$$

For $v_0 = 0$ and only one cell ϕ the resulting system of equations is a surface Cahn-Hilliard equation on a bendable surface. It relates to phase-field approximations of a Jülicher-Lipowsky model for two-component vesicles [52, 60, 61]. However, there are conceptual differences. These models only consider one spatial scale and a bending rigidity $\kappa_{bending} = \kappa_{bending}(\phi)$ with a functional dependency on ϕ . This not only requires to consider $\mathcal{F}_{Helf} + \mathcal{F}_{CH}$ instead of \mathcal{F}_{Helf} in eqs. (2) - (4), but also $\mathcal{F}_{Helf} + \mathcal{F}_{CH}$ instead of \mathcal{F}_{CH} in eq. (8). In our context we can make use of the two-scale character. Due to separation of scales we question the necessity of \mathcal{F}_{CH} and \mathcal{F}_{Int} to be considered in eqs. (2) - (4). Both are essentially only nonzero within the vicinity of the cell interfaces and thus on a small scale, which is not relevant for the large scale surface evolution. We therefore neglect these terms in eqs. (2) - (4). Instead

of a functional dependency of the bending rigidity $\kappa_{bending} = \kappa_{bending}(\phi_1, \dots, \phi_N)$ on all phase-field variables, which would require to consider $\delta\mathcal{F}_{Helf}/\delta\phi_i$ in eq. (8), we interpret $\kappa_{bending}$ as a coarse-grained parameter addressing only topological features of the monolayer. The implicit dependency of these features on ϕ_i will be neglected in eq. (8), the same holds for the resulting spatial dependency in eqs. (2)-(4). Considering these approximations the coupled system eqs. (2)-(5), (8), (9) and (11) remain without further modification.

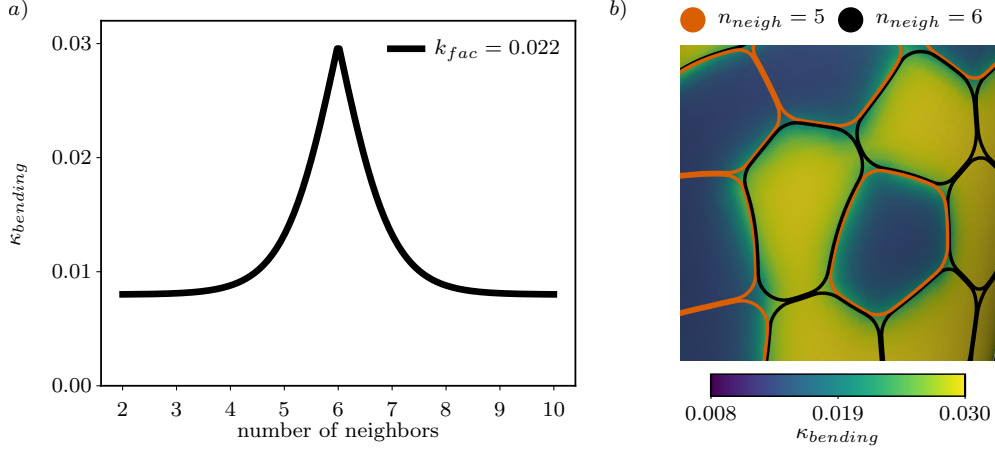


Fig. 2 Bending rigidity $\kappa_{bending}$ as a function of the number of neighbors n_{neigh} for $k_{fac} = 0.022$ and $k_{lower} = 0.008$, shown as graph in a) and a numerical realization showing the cell contours color-coded by the number of neighbors and the values of $\kappa_{bending}$ in b).

Various examples exist in which material properties are influenced by topological defects resulting from the underlying microstructure. Such features are well studied in flat space [51, 62], but have also been found in spherical surfaces [39]. Related to these features is the number of neighbors of a cell. Due to Euler's polyhedron formula, for the topology of a sphere there must be cells with the number of neighbors deviating from six. The neighbor distribution and the optimal arrangement of interacting cells on a sphere are a well studied problem. Depending on the number of cells, disclinations, isolated cells with five or seven neighbors, dislocations, pairs of five- and seven-fold disclinations, or grain boundary scars, chains of five- and seven-fold disclinations, emerge. Most studies consider fixed, e.g., circular cells, but the same phenomena can also be found for deformable cells [39]. Material properties differ at these topological defects, they are sources for weakness. We therefore modify the bending rigidity for these cells. The considered dependency reads

$$\kappa_{bending}(\mathbf{x}, t) = k_{fac} (\tanh(-|n_{neigh}(\mathbf{x}, t) - 6|) + 1) + k_{lower} \quad (12)$$

with parameters k_{fac} and k_{lower} determining the maximal values for cells with six neighbors and the minimal values which is approached for increasing deviations from six. $n_{neigh}(\mathbf{x}, t)$ is the number of neighbors of the cell, which center of mass is closest

to position \mathbf{x} at time t . We call two cells neighbors if their diffused interfaces overlap, so if they are able to interact. To be precise we follow [63] and say two cells are neighbors if $\{\phi_i|\phi_i > -0.5\} \cap \{\phi_j|\phi_j > -0.5\} \neq \emptyset$. The dependency of $\kappa_{bending}$ on n_{neigh} is phenomenological and chosen similar to the discrete defect localization approach in [64], where it was shown to lead to qualitatively similar results than variational based approaches [25, 64]. The functional form and a realization for selected cells in a cell monolayer after numerical smoothing, see Section 2.4, are shown in Figure 2.

2.4 Discretization

The overall system of geometric and surface partial differential equations is solved by surface finite elements in space [18, 58] and classical finite differencing in time. We consider an operator splitting approach to decouple the Lagrangian movement in normal direction and the Eulerian evolution in tangential direction in each time step. For each subproblem we build on established approaches.

In order to numerically solve eqs. (2)-(4) we follow [65]. As in [14, 52] we supplement these equations with an additional equation for the time evolution of the parametrization. We consider the initial surface given $\mathbf{X}(0) = \mathbf{X}_0$ and solve

$$\partial_t \mathbf{X} \cdot \mathbf{n} = v_n \tag{13}$$

$$H\mathbf{n} = \Delta_{\mathcal{C}} \mathbf{X}. \tag{14}$$

This generates a tangential mesh movement that maintains the shape regularity and additionally provides an implicit representation of the mean curvature H [65]. Eqs. (2)-(4) and eqs. (13) and (14) are solved together. We approximate the smooth surface $\Gamma(t)$ by a discrete k -th order approximation $\Gamma_h^k(t)$ [66] and consider each geometric quantity, like the normal \mathbf{n}_h , the shape operator \mathcal{B}_h and the inner product $(\cdot, \cdot)_h$ with respect to $\Gamma_h^k(t)$. In the following we drop the index k . We define the discrete function spaces by $V_l(\Gamma_h) = \{\psi \in C^0(\Gamma_h) | \psi|_T \in P_l(T)\}$ with P_l the space of polynomials and T the element of the surface triangulation. We define $\mathbf{V}_l(\Gamma_h) = [V_l(\Gamma_h)]^3$ as space of discrete vector fields and consider $\mathbf{X}_h \in \mathbf{V}_2(\Gamma_h)$ and $H_h, \kappa_{bending,h} \in V_2(\Gamma_h)$. For a detailed weak and finite element formulation we refer to [14, 52]. In order to obtain the same numerical properties and convergence behavior as in these approaches we smooth $\kappa_{bending,h}$ by solving one pseudo time step of $\partial_t \kappa_{bending,h} = \Delta_{\Gamma} \kappa_{bending,h}$.

For solving eqs. (8), (9) and (11) we extend the approach introduced for the problem in flat space [67] and considered on fixed curved surfaces [39, 40] to evolving surfaces. Based on $\Gamma_h(t)$, which serves as a macro mesh we consider N different refinements $\Gamma_{h,i}(t)$ to resolve the N phase-field variables ϕ_i . This multimesh approach [67] allows to solve the N problems in parallel. Only interactions between cells require communication, which is done on the only virtually available common finest mesh of the different refinements. In flat space this approach is shown to scale with the number of cells N [67]. In our context the approach also resamples the two-scale nature of the problem. All geometric properties of the surface are only communicated on the common macro mesh $\Gamma_h(t)$. We split the fourth order systems into coupled systems of second order problems by defining $\mu_i = \delta(\mathcal{F}_{CH} + \mathcal{F}_{Int})/\delta\phi_i$ and consider

$\phi_{i,h}, \mu_{i,h} \in V_2(\Gamma_{h,i})$. A detailed weak and finite element formulation on stationary surfaces can be found in [40]. For the extension to evolving surfaces we follow [52]. We essentially consider the relative material velocity as \mathbf{w}_h^n in the material time derivative.

With these two subproblems set the overall algorithm starts with an initial parametrization $\mathbf{X}_h(0)$, phase-field variables $\phi_{i,h}(0)$ and chemical potentials $\mu_{i,h}(0)$ and evolves in time from t^n to t^{n+1} by first computing $\kappa_{bending,h}^n$ using $\phi_{i,h}^n$ and solving the geometric evolution problem for v_n^{n+1} , λ_{area}^{n+1} , λ_{vol}^{n+1} , \mathbf{X}_h^{n+1} and H_h^{n+1} and afterwards solve the system of surface partial differential equations for $\phi_{i,h}^{n+1}$ and $\mu_{i,h}^{n+1}$ using v_n^{n+1} , \mathbf{X}_h^{n+1} and H_h^{n+1} . The approach is implemented in AMDiS [68–70] which is based on the DUNE library [71, 72]. For the surface approximation DUNE-CurvedGrid [66] together with DUNE-AluGrid [73] is used. For $v_0 = 0$, only one phase ϕ and a stronger constraint on the conservation of area the approach is shown to converge for $e_{\mathbf{X}} = \|\mathbf{X}_h - \mathbf{X}\|_{L^\infty(L^2(\Gamma_h))}$ and $e_\phi = \|\phi_h(\mathbf{X}_h) - \phi(\mathbf{X})\|_{L^\infty(L^2(\Gamma_h))}$ experimentally with optimal order [52, 61]. We rely on these results and refrain from further convergence studies, which, due to the complexity of the problem for $N \gg 1$, also become unfeasible.

Further technical details and the considered parameters are listed in the Appendix.

3 Results

3.1 Comparison with classical Canham/Helfrich model

We first test the problem for consistency and set $v_0 = 0$. For $\kappa_{bending} = const$ the shape evolution reduces to the classical Canham/Helfrich problem [41, 42]. The preferred shapes arise from a competition between the Canham/Helfrich energy and the geometrical constraints on fixed surface area and fixed enclosed volume. These shapes of lowest energy can be classified in phase diagrams, which in the considered parameter regime show two stable branches of prolate and oblate shapes [74]. Figure 3 shows the computed diagram together with sample shapes for selected values of the reduced volume, which denotes the scaled quotient of the enclosed volume and the surface area $V_r = 6\sqrt{\pi}|\Omega|/|\Gamma|^{3/2}$. A reduced volume $V_r = 1$ thus corresponds to a sphere. The phase diagram agrees with [74], where the shapes are computed in an axisymmetric setting.

3.2 Consistency tests for passive system

In the next step we are interested in how these shapes deform if the surface consists of cells and the proposed form $\kappa_{bending}$ in eq. (12) is used. We consider two cases $N = 12$ and $N = 32$. The optimal arrangements of 12 and 32 interacting cells on a sphere are known. Finding these arrangements is related to the classical Thomson problem for the interaction of points on a sphere [75] and the Tammes problem, which asks for the positions such that the minimum distance between points is maximized, which is equivalent to the optimal packing of circles on the sphere [76]. For $N = 12$ the results are known and identical. The points reside at the midpoints of the faces of a regular dodecahedron. For $N = 32$ the minimal energy configurations form a truncated icosahedron. Also in this situation the topology of the minimal configurations, which

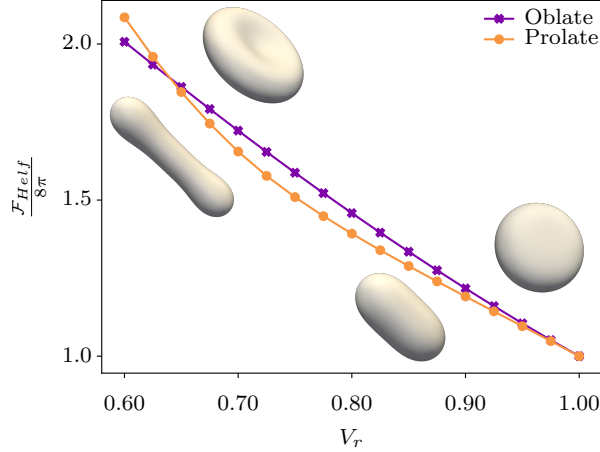


Fig. 3 Rescaled bending energy $\mathcal{F}_{Helf}/(8\pi)$ of minimal energy configurations as function of reduced volume V_r together with sample shapes for $\kappa_{bending} = 1.0$. The sample shapes correspond to $V_r = 0.65$ (left) and $V_r = 0.9$ (right) and show the oblate (top) and prolate (bottom) configuration.

resamples a classical soccer ball, agrees for both problems. The robustness of these configurations with respect to the specific interaction potential has also been demonstrated numerically, see [77, 78] for an approach based on a surface phase-field crystal model. We therefore expect to find these configurations also for our problem. As for an initial sphere the shape remains fixed, due to the area and volume constraint, the problem significantly simplifies and has already been solved in [39]. Indeed for these special cases the expected configurations are obtained. Starting from these configurations we now reduce the enclosed volume, keep the surface area fixed and relax the system by solving the full problem with $v_0 = 0$. While for $N = 12$ all cells have initially 5 neighbors and thus $\kappa_{bending} = const$, for $N = 32$ we have 12 cells with five neighbors and 20 cells with six neighbors and thus variations in $\kappa_{bending}$. We therefore expect to see changes in the emerging equilibrium configurations. Figure 4 shows the obtained minimal energy configurations for selected values of the reduced volume V_r .

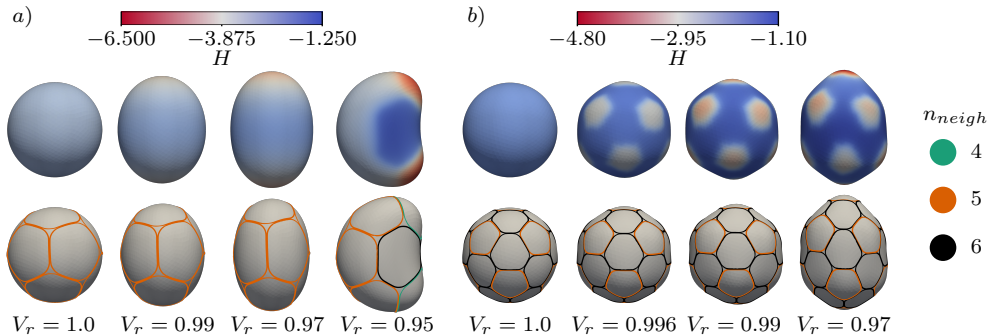


Fig. 4 Equilibrium energy configurations for selected reduced volumes V_r and $N = 12$ a) and $N = 32$ b). Top row shows the mean curvature H and bottom row the contours of the cells, color coded according to the number of neighbors.

For $N = 12$, see Figure 4 a), above some threshold for $V_r \approx 0.96$ the obtained shapes resample the equilibrium shapes of the prolate branch from Figure 3. This is a consequence of the definition of $\kappa_{bending}$ in eq. (12) which is homogeneous if the number of neighbors is constant for all cells. However, below this threshold the influence of the shape on the cells becomes apparent. Due to the two emerging strong curvature regions of the prolate the cells deform and rearrange, which leads to variations in the number of neighbors and thus heterogeneity in $\kappa_{bending}$. This breaks the symmetry and forms a new (local) equilibrium shape not seen in Figure 3. For $N = 32$, see Figure 4 b), the inhomogeneity in $\kappa_{bending}$ leads to symmetry breaking for all $V_r < 1.0$. Above some threshold, $V_r \approx 0.99$, the surface approaches the shape of a truncated icosahedron. The topology of cell arrangement remains but the curvature is increased at cells with five neighbors. Such configurations have also been found in [64], which combines a surface phase-field crystal model with bending properties of the surface and a similar multiscale coupling to model the buckling instability in viral capsids. The obtained shapes deviate from the simple prolate or oblate shapes for $\kappa_{bending} = const$ in Figure 3. Further reducing V_r makes these truncated icosahedral shapes unfeasible and leads to further symmetry breaking and prolate-like shapes. The geometric axis of the prolate thereby emerges from one of the six symmetry axis determined by the positions of the cells with five neighbors. But also in these configurations cells with five neighbors are located in, or form, regions of high curvature, only the magnitude now differs and is largest at the cells at the symmetry axis of the prolate. This transition can be quantified by measuring the distance between opposed cells with five neighbors and the mean angle these axis form with each other, see Figure 5. In these plots the deviation of one axis, the symmetry axis of the prolate, from all others is shown. The other five axis behave similar and only slightly decrease (length) or slightly increase (mean angle), as a geometric consequence of the volume and area constraints. For a sphere, $V_r = 1.0$, the values are equal and for the angle approximate the known quantity for a regular truncated icosahedron of $\arccos\left(\frac{1}{\sqrt{5}}\right) \approx 63.43^\circ$.

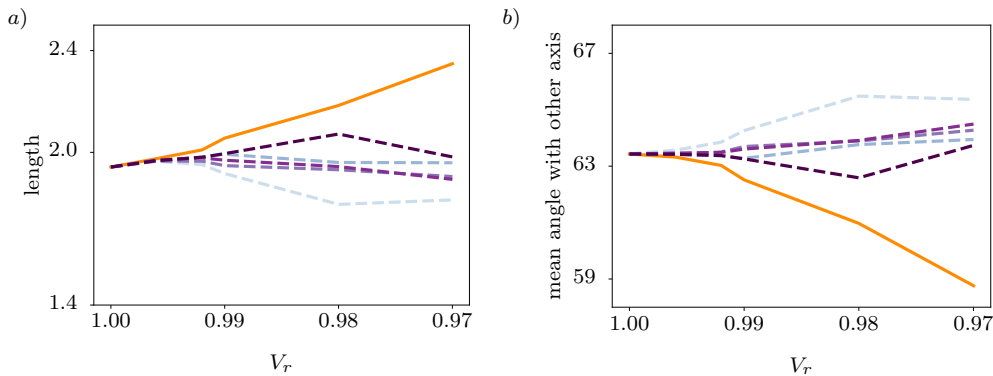


Fig. 5 Symmetry breaking for $N = 32$. Reducing the reduced volume V_r leads to truncated icosahedral shapes for $V_r \gtrsim 0.99$ (all six axis connecting opposed cells with 5 neighbors behave similar) and prolate like configurations for $V_r \lesssim 0.99$ (one axis (solid, orange) deviates from the others (dashed)). Shown is the distance between the cells a) and the mean angle with the other axis b) as functions of the reduced volume V_r .

3.3 Effect of activity

In the next step we consider these equilibrium configurations and add activity by setting $v_0 > 0$. For a sphere, $V_r = 1$, this resamples the situation considered in [39], where collective rotation was discovered as an intermediate phase between the solid and liquid phase of the tissue if the number of cells is small and the activity not too large. We consider the case $N = 12$ and a similar parameter regime but now for reduced volumes $V_r < 1.0$. Figure 6 shows some of the results. For $V_r \gtrsim 0.96$ we obtain the same behavior as in [39]. Cells collectively rotate. Figure 6 a) shows overlaid cell contours of three cells for different time instances indicating their movement. The corresponding trajectories of the centers of mass of these cells are shown in Figure 6 b). Both indicate collective rotation on a fixed shape. The direction of rotation depends on the initialization of \mathbf{e}_i , which are initialized from a random uniform distribution.

For $V_r \lesssim 0.96$ the situation changes, see Figure 6 c). Instead of collective rotation on a fixed shape the results indicate that the shape rotates and the cells are transported with the shape. Similar phenomena of rigid body rotations have been observed in models for fluid deformable surfaces [15, 79, 80]. Such models consider the tangential motion of the cells as a continuous surface fluid [12–14]. To further confirm these different behaviors we quantify the shape of the cells and the surface for both cases. The first is considered using surface Minkowski tensors [81]. These tensors characterize rotational symmetries of shapes embedded in curved surfaces and are extensions of classical Minkowski tensors in integral and stochastic geometry [82]. We here consider the normalized eigenvalues of the irreducible surface Minkowski tensors μ_p as a shape measure for the cells, see [81] for details. The index p denotes the symmetry under rotations by $\frac{2\pi}{p}$ with p being an integer. Briefly, $\mu_p \in [0, 1]$ with $\mu_p = 1$ for a regular geodesic polygon with p vertices, which, however, might not exist on general surfaces. Surface Minkowski tensors are translation and scaling invariant, which on the surface translates to invariance under any flow generated by a Killing vector field and invariance under constant conformal changes of the metric of the surface, respectively. Furthermore, as also shown in [81], they are robust against small perturbations of the shape of the cells or the surface. These properties allow to compare the shape of the cells on surfaces, even if they experience different geometric properties. As all cells, at least on the prolate in Figure 6 a) and b), have five neighbors, we expect an established five-fold symmetry also for the individual cells. For computational issues concerning μ_p see Appendix.

In order to quantify the shape of the surface we consider global shape classifications using spherical harmonic-based principal component analysis, a method researched in depth in the fields of 3D-particle morphology and surface reconstruction [83, 84] as well as in computer graphics [85]. For this method the surface is expressed as function r_{SH} on the unit sphere S^2 following [84], whereby the origin is used as a reference point. This requires a restriction to star-like shapes (with respect to the origin). Then every point on the surface can be uniquely associated to two angles (θ, φ) so that $\mathbf{X}(\theta, \varphi)$ is the point of the surface that we reach when we go from the origin in the direction $(\cos(\varphi) \sin(\theta), \sin(\varphi) \sin(\theta), \cos(\theta))^T$. Note that the star like shape ensures

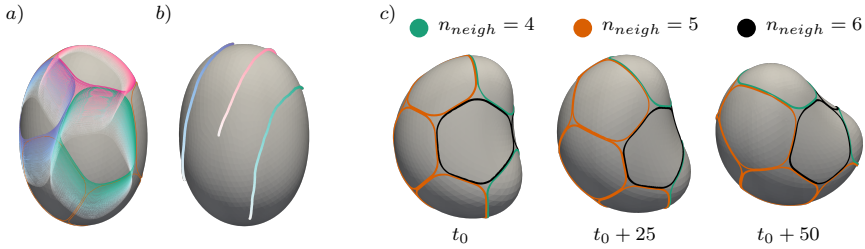


Fig. 6 Collective rotation for $N = 12$ and $v_0 = 0.16$. For $V_r = 0.97$ (Outlines from subsequent timesteps shown in a), Trajectories shown in b)) the cells rotated collectively, without changing the shape of the surface. For $V_r = 0.95$ the collective rotation of the cells leads to an rotation of the surface as shown in the snapshots in c).

the uniqueness of the association. With this we define:

$$r_{SH}(\theta, \varphi) = \|\mathbf{X}(\theta, \varphi)\|_2 \quad (15)$$

As the surface is now described by a scalar function on the unit sphere and as the spherical harmonics are an orthonormal basis on the sphere we can now write this as

$$r_{SH}(\theta, \varphi) = \sum_{l=0}^{\infty} \sum_{m=-l}^l q_l^m Y_l^m(\theta, \varphi) \quad (16)$$

where we can calculate q_l^m with

$$q_l^m = \int_{S^2} r_{SH}(\theta, \varphi) \overline{Y_l^m(\theta, \varphi)}, \quad (17)$$

where $\overline{\{\dots\}}$ denotes the complex conjugate. To characterize and analyze the surface only the coefficients with $l \leq 12$ are regarded as this turned out to be sufficient to describe the general shape of a surface [86], see also Figure 17 in Appendix for a convincing example. To get a rotation invariant measure we follow [85] and introduce

$$q_l = \sum_{m=-l}^l (q_l^m)^2 \quad (18)$$

and for a scale invariant measure we consider

$$\tilde{q}_l = \frac{q_l}{\sum_{l=0}^{l_{max}} q_l} \approx \frac{q_l}{\int_{S^2} r_{SH}(\theta, \varphi)^2} \quad (19)$$

following [85, 87].

Due to the rotational invariance of q_l our shape measures stay constant, as can be seen in Figure 7 a) (for $V_r = 0.97$, which corresponds to Figure 6 a) and b)) and Figure

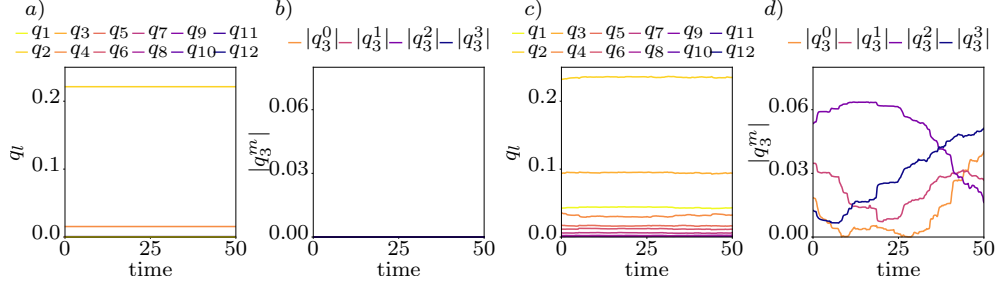


Fig. 7 Surface shape quantifiers q_l for $N = 12$ and $v_0 = 0.16$. For $V_r = 0.97$ q_l are shown in a) and $|q_3^m|$ in b), for $V_r = 0.95$ q_l are shown in c) and $|q_3^m|$ in d). The axis scaling between a) and c) as well as b) and d) respectively is kept constant.

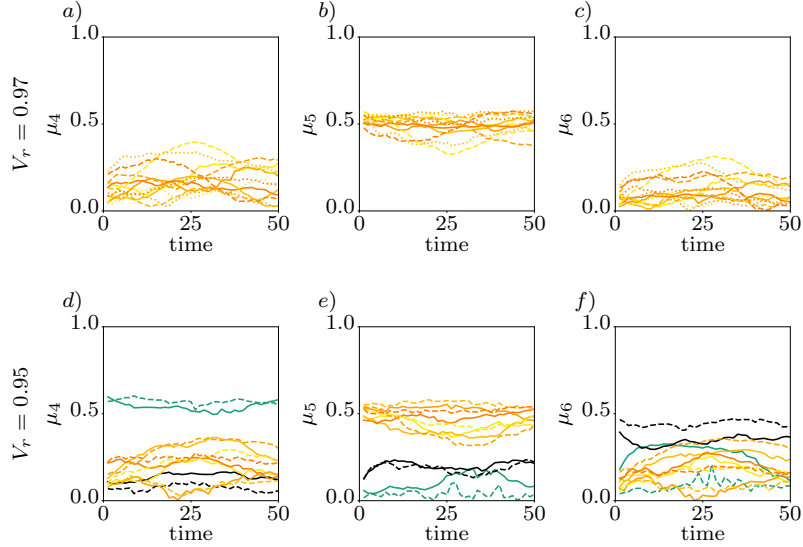


Fig. 8 Cell shape measures μ_p for $N = 12$ and $v_0 = 0.16$. For $V_r = 0.97$ μ_4 are shown in a), μ_5 in b) and μ_6 in c). For $V_r = 0.95$ the corresponding data is shown in d), e) and f), respectively. For each cell μ_p is shown over time. The line is colored according to the number of neighbors, whereby different line styles are used to distinguish different cells with the same number of neighbors. Furthermore different shades of yellow and orange are used for cells with 5 neighbors.

7 c) (for $V_r = 0.95$, which corresponds to Figure 6 c)). If we take a closer look at q_l^m , here for $l = 3$, which are not rotation invariant, one can see that they are still constant for $V_r = 0.97$ (see Figure 7 b)) while they are changing for $V_r = 0.95$ (see Figure 7 d)). This confirms the postulated differences between Figure 6 a) and b) (collectively rotating cells without changing the shape of the surface) and c) (collective rotation of the cells leading to rotation of the surface).

We now concentrate on the cell level and consider the irreducible surface Minkowski tensors μ_p to quantify the shape of the cells. Results are shown in Figure 8. For $V_r = 0.97$ (see Figure 8 a) - c)) and $V_r = 0.95$ (see Figure 8 d) - f)) we see a connection between the number of neighbors and the values of μ_p . For example for $V_r = 0.97$,

where all cells have five neighbors, all cells have similar values for μ_5 , see Figure 8 b), which are also significantly larger than the values for μ_4 and μ_6 , see Figure 8 a) and c), respectively. A similar behavior can be observed for $V_r = 0.95$. Here the behavior depends on the considered cells. For cells with four or five neighbors (see Figure 8 d) and e), respectively) the values for μ_4 and μ_5 are larger and stay roughly constant. Small shape changes, resulting from the random character of the incorporated activity, are expected. However, the overall behavior remains in a dynamic equilibrium not changing the global arrangement. At least for $V_r = 0.97$, where the cells collectively rotate on a prolate the cells experience different curvatures, see the selected cell trajectories in Figure 6 b). While this modifies the shape of the cells it only has a minor influence on the five-fold rotational symmetry, see Figure 8 b). Only for the lower values of μ_4 and μ_6 in Figure 8 a) and c), respectively, fluctuations in time, which relate to the rotation, emerge.

3.4 Two-scale coupling for more cells

With the results of the considered problems with small numbers of cells, which resample known results and already demonstrate the possibility of new phenomena emerging from the two-scale coupling, we now turn to the full problem and consider $N = 92$. While still much lower than the envisioned problems in morphogenesis, the considered setting remains computational feasible and allows for statistical investigations. Figure 9 shows snapshots of the evolution. The corresponding equilibrium shape for $\kappa_{bending} = const$ and a random arrangement of cells was used as initial configuration.

In all cases the shape evolves away from the equilibrium shape. Cells migrate and deform, due to interactions with other cells but also by experiencing different geometric properties of the evolving shape. Events can be identified where cells move relative to each other through structural rearrangements. This changes the number of neighbors and therefore the bending rigidity $\kappa_{bending}$ which has an effect on the shape evolution, which is less regular than simulation results for continuous models, e.g., for active fluid deformable surfaces [15]. For further comparison with such continuous approaches we also consider the surface velocity. To obtain a global velocity field we compute a velocity for each cell considering the centers of mass at the time instances t and $t + 5.0$. These velocities are summed up, whereby the rescaled phase-field of the respective cell is used as a weight. Afterwards the global field is smoothed with a linear interpolation kernel whereby the radius of this kernel corresponds to the radius of the cell. The corresponding velocity fields to Figure 9 at time $t = 25$ are shown in Figure 10. Two different ways to visualize the surface velocity are considered, the first focuses on the global velocity \mathbf{v}^{cell} (Figure 10 a)) and the second decomposes it into its tangential and normal components $\mathbf{v}^{cell} = \mathbf{v}_{tangential}^{cell} + v_{\mathbf{n}}\mathbf{n}$ and visualizes both components (Figure 10 b)). As for simulations of fluid deformable surfaces [13, 14] the normal and tangential velocity components are tightly coupled. Any shape change induces deformations of the cells and thus a tangential flow. Rearrangement of cells modifies the bending rigidity and induces local shape deformations thereby creating local gradients of mean curvature. Such gradients are of special interest as they are proposed as sources of active geometric forces [11, 15, 88]. The generation of gradients

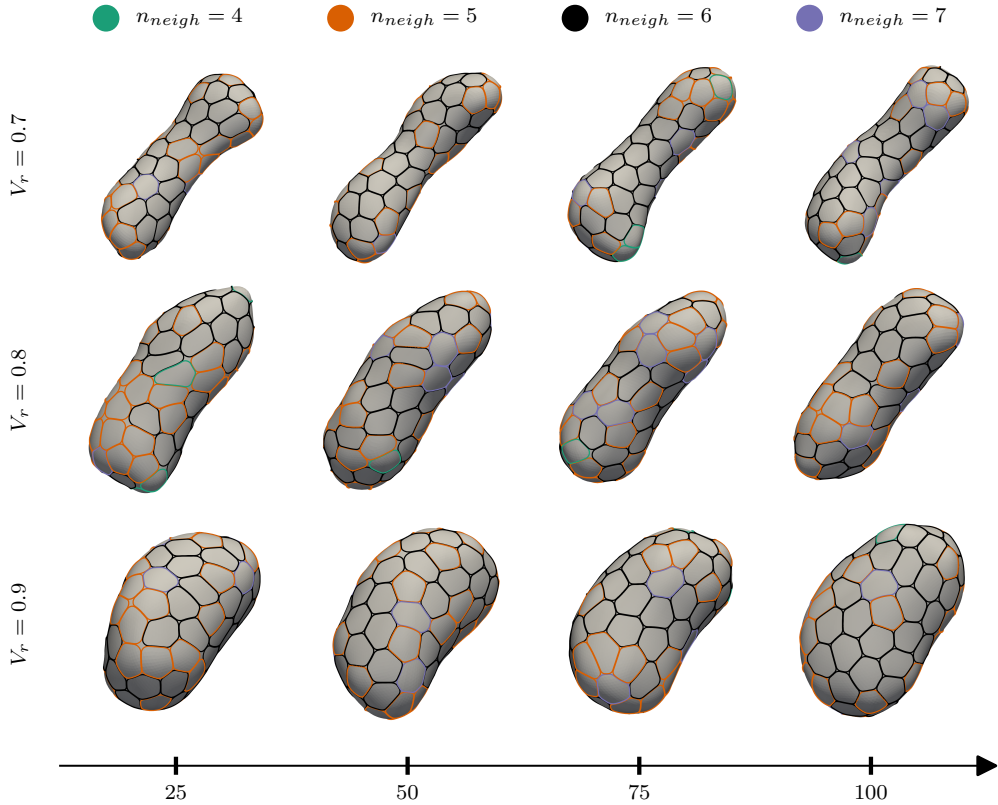


Fig. 9 Shape evolution for $N = 92$ and $v_0 = 0.2$ and different reduced volumes V_r . The cells are color coded according to the number of neighbors. The evolution is shown after an initialization phase.

in mean curvature thus might be an initialization for larger shape changes as observed in morphogenesis.

To analyze such evolutions and explore how the resulting shape changes depend on activity on the cellular scale we measure local and global geometric properties. We first compute the mean curvature H and the gradient of the mean curvature $\nabla_{\Gamma} H$ at each point and time step and consider the average values. Figure 11 shows the resulting values as a function of the reduced volume V_r and for different values of the activity v_0 in comparison to the equilibrium prolate shape.

As expected the averaged mean curvature decreases (negative sign for $\langle H \rangle$) and the averaged gradient of the mean curvature increases for decreasing V_r , indicating the stronger deviation from a sphere. The strength of the activity has only a minor effect. While the averaged mean curvature essentially reproduces the properties of the equilibrium shape, the average mean curvature gradient strongly deviates. This results from the properties of the bending rigidity. Local variations in the bending rigidity lead to changes in mean curvature.

Besides these averaged local geometric quantities we are also interested in a potential correlation between the mean curvature H and the number of neighbors of the

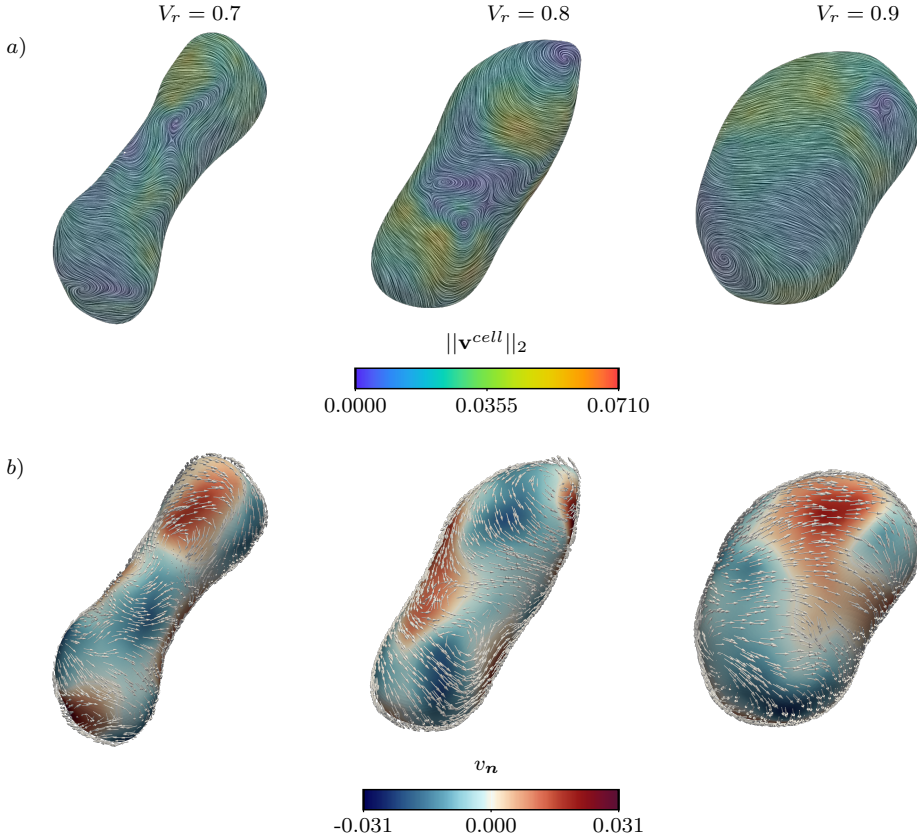


Fig. 10 Global velocity field for simulations with $N = 92$ and $v_0 = 0.2$ and different V_r at time $t = 25$. a) LIC (line integral convolution) filter with color coding according to the magnitude of the global velocity field. b) Decomposed global velocity in its normal and tangential components. The magnitude of the normal part is color-coded. Thereby blue indicates movement inwards and red movement outwards. The direction of the tangential velocity field is shown by arrows, with length corresponding to the magnitude of the tangential velocity in log-scale.

cells n_{neigh} . We therefore compute the mean number of neighbors and its standard deviation. Both quantities are shown in Figure 12 as a function of the reduced volume V_r and for different values of the activity v_0 . The corresponding distributions are shown in Figure 13 as histograms. While the values only slightly change with V_r the mean number of neighbors decreases towards five with increasing v_0 , which is associated with an increase in the standard deviation. In flat space the associated neighbor distributions are very robust. They are always centered at six and a broadening with activity is well known [57], which is also observed here. A shift of the mean value towards five furthermore is consistent with results on a sphere [39]. The shift towards five and the broadening of the distribution leads to a strong increase in the number of topological defects and with it an increase in heterogeneity of the bending rigidity $\kappa_{bending}$, which on average becomes weaker. The increase in heterogeneity with

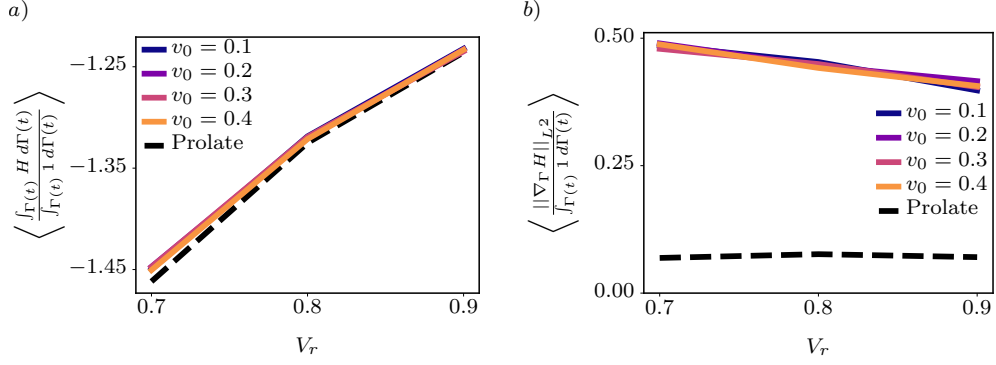


Fig. 11 Local geometric properties. a) Averaged mean curvature $\langle H \rangle$ and b) averaged mean curvature gradient $\langle \|\nabla_{\Gamma} H\|_{L^2} \rangle$ as functions of the reduced volume V_r for different activities v_0 . The dashed line shows the values for the equilibrium prolate shapes from Figure 3.

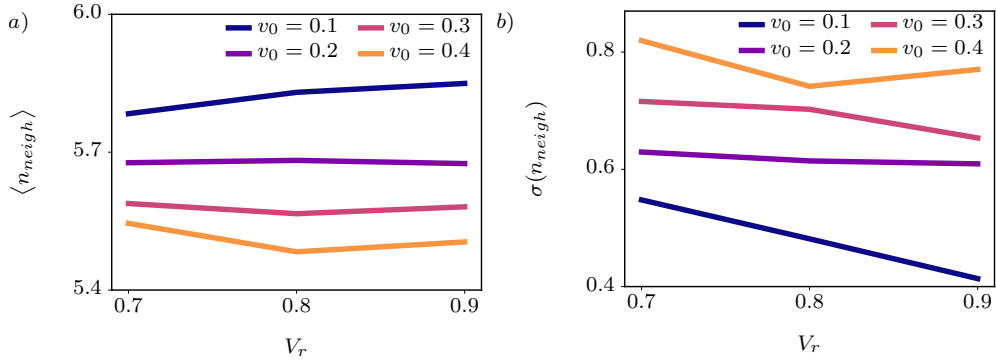


Fig. 12 Number of neighbors: a) Mean number of neighbors $\langle n_{neigh} \rangle$ and b) standard deviation $\sigma(n_{neigh})$ as function of the reduced volume V_r for different activities v_0 .

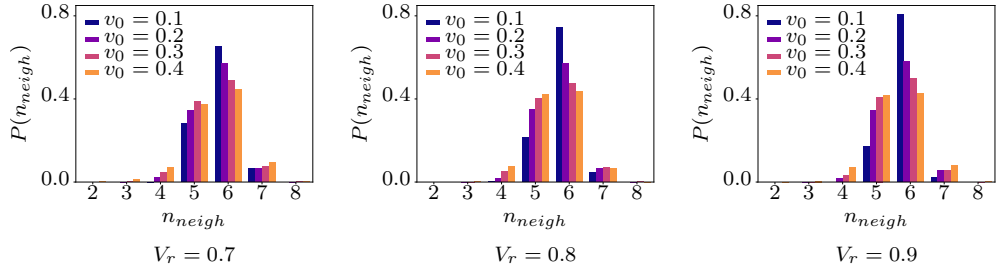


Fig. 13 Distribution of the number of neighbors n_{neigh} for different reduced volumes V_r and different activities v_0 .

respect to neighbor relations correlates with a shift from dominating six-fold to five-fold rotational symmetry. This can be quantified by computing the irreducible surface Minkowski tensors μ_5 and μ_6 , see [81], for all cells and computing their average, which are shown in Figure 14.

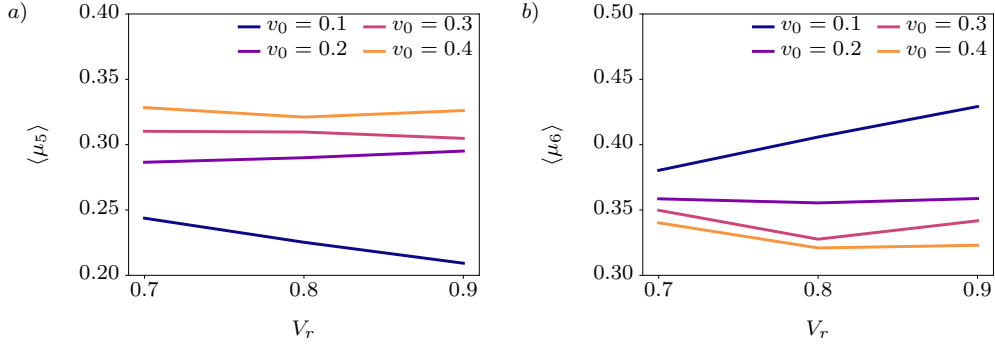


Fig. 14 Averaged irreducible surface Minkowski tensors μ_p . a) $p = 5$ and b) $p = 6$ for all cells as functions of the reduced volume V_r for different activities v_0 .

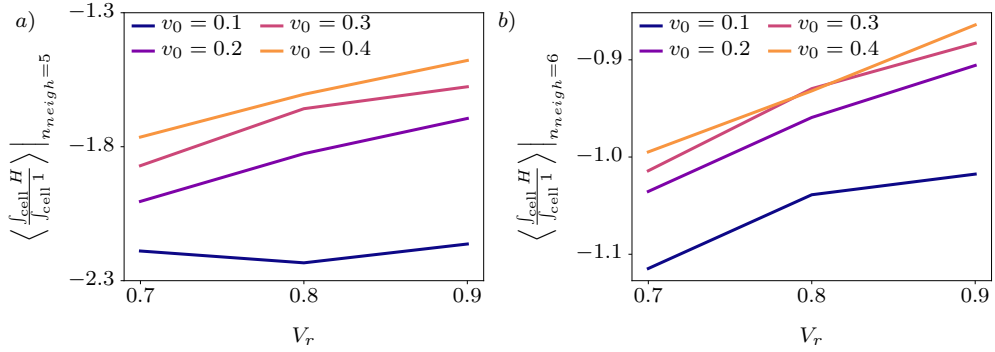


Fig. 15 Local geometric properties at specific cells: a) Average mean curvature $\langle H \rangle$ for all cells with five neighbors and b) average mean curvature $\langle H \rangle$ for all cells with six neighbors as function of the reduced volume V_r for different activities v_0 .

We next relate the number of neighbors n_{neigh} and the mean curvature H to each other. Figure 15 shows the average value of the mean curvature at cells with five and cells with six neighbors in a) and b), respectively. Other numbers n_{neigh} , while rarely present, do not allow for meaningful statistics and are therefore not discussed. Again the data is shown as a function of the reduced volume V_r and for different activities v_0 . Both quantities consistently decrease (negative sign for $\langle H \rangle$) with decreasing V_r and increase with increasing v_0 . However, the values for cells with five neighbors are significantly lower (negative sign for $\langle H \rangle$) than the once for cells with six neighbors. The absolute difference between these values decreases with increasing v_0 .

At last we aim to quantify global shape changes. For this purpose we consider the shape measures \tilde{q}_l . We consider two quantities, the first considers the average change of the shape in a fixed time unit, here 0.125, and the second the average change with respect to the initial prolate shape. These quantities read

$$\text{relative shape change} = \frac{1}{n_{timestep}} \sum_{t^n} \sqrt{\sum_0^{l_{max}} (\tilde{q}_l(t^n + 0.125) - \tilde{q}_l(t^n))^2} \quad (20)$$

$$\text{absolute shape change} = \frac{1}{n_{\text{timestep}}} \sum_{t^n} \sqrt{\sum_0^{l_{\text{max}}} (\tilde{q}_l(t^n) - \tilde{q}_l(0))^2}, \quad (21)$$

where n_{timestep} is the number of time steps and t^n the n -th time instant. These quantities increase with decreasing reduced volume V_r , which can be explained by the enlarged shape space which is explored by the evolution. The dependency on activity v_0 is more subtle: The relative shape change increases with activity while the absolute shape change decreases. This corresponds to larger shape fluctuation on short time scales but less deviations from the equilibrium configurations over long time scales. Activity thus allows to explore the shape space but also to approach shapes close to equilibrium. A property which had also been found numerically for active fluid deformable surfaces [15]. However, here it is also a consequence of the considered activity, which contains a random component. Furthermore the constraints on area and enclosed volume of the global shape restrict strong deviations. The last aspect considers the time evolution. While stronger activities lead to more heterogeneity and stronger tangential motion, the relaxation in normal direction is not directly effected. This might result in situations where the shape has not enough time to adapt to local changes in bending rigidity before neighbor relations are changed again.

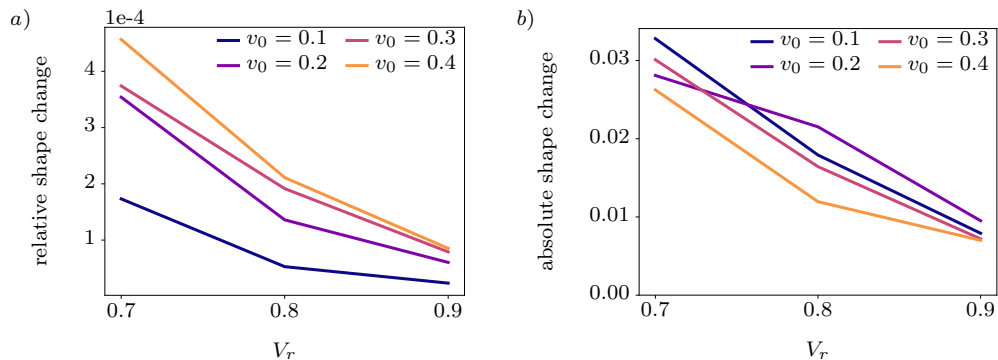


Fig. 16 a) Relative shape change with respect to consecutive time instances and b) absolute shape change with respect to initial prolate shape for $N = 92$ and the considered time period $t^n \in [10, 99.775]$ as function of the reduced volume V_r for different values of the activity v_0 .

4 Discussion

Large-scale motion in developmental tissue deformations emerges from collective tissue-mechanical properties of multicellular structures. Unfortunately these properties on the tissue scale are largely unknown, which limits predictive quantitative simulations of morphogenetic processes. As one step to overcome this limitation we have proposed a two-scale modeling approach in which each individual cell is resolved and the properties on the tissue scale do not need to be imposed but emerge from the interactions of the cells. This shifts the problem to providing mechanical properties

of the cells. To construct a computationally feasible model requires various modeling assumptions. We have made use of scale separation to decouple processes on the cellular and tissues scale as much as possible and only consider the simplest possible model for a deformable cell. One of the coupling mechanisms is in the definition of the bending rigidity of the tissue, which locally depends on the topology of the cellular network. Being inspired by thin crystalline sheets, which buckle at defects, the bending rigidity is reduced if cells have less or more than six neighbors. Using advanced software tools, which essentially scale with the number of cells on parallel architectures, the features of the proposed two-scale model have been explored.

For small numbers of cells and spherical shapes ($V_r = 1.0$), which resample epithelial acini [89, 90], we observed collective rotation, as in [39]. However, this changes if the reduced volume V_r is reduced. Below some threshold the motion turns from a collective motion on a more or less stationary shape to a rigid body rotation, where the cells more or less remain stationary but collectively rotate the global shape. Activity on the cellular level thus not only leads to collective motion in form of tangential flow but also to shape deformations of the tissue. The resulting shapes have broken symmetries, which strongly depend on the topology of the cellular arrangement. These configurations show larger absolute values of the mean curvature at topological defects. For larger numbers of cells we have analyzed averaged quantities. We found global flow patterns, which show a tight coupling between the tangential $\mathbf{v}_{\text{tangential}}^{\text{cell}}$ and the normal velocity $v_{\mathbf{n}}$ components, reminiscent to fluid deformable surfaces [12, 13]. An other finding was a strong increase in gradients of the mean curvature $\nabla_{\Gamma} H$ if compared with the equilibrium prolate shape. This results from the change in bending rigidity and can also be seen in classical two-component models on membranes with a phase-dependent bending rigidity, e.g., [52, 91–93]. However, here it appears on the cellular scale and might be a mechanism to initiate active geometric forces [11, 15, 88], which require gradients in mean curvature. Other findings are concerned with the number of neighbor distribution, which slightly broadens with decreased reduced volume V_r and increased activity v_0 and also shifts towards five for the mean value if V_r is decreased or v_0 is increased. We thus obtained an increase in heterogeneity and associated with this a weakening of the bending properties of the tissue. These neighbor relations correlate with the rotational symmetry properties of the cells, which have been computed using irreducible surface Minkowski tensors [81].

While all these results remain qualitative, they demonstrate the influence of the cellular scale on large scale tissue deformations. The approach provides a way to incorporate activity on the level it is generated. In principle this opens up possibilities to also consider sub-cellular processes, even genetic and mechano-chemical processes. However, modeling assumptions on the cellular scale are expected to have an impact on the shape evolution. We here considered the simplest possible model for a cell. As already seen in flat space assumptions on the motility mechanism lead to different mechanical properties of the tissue [36]. Also extrinsic curvature effects, which lead to an alignment of the cells with principal curvature directions of the underlying surface [40, 94] have been neglected. Other strong assumptions are the constant cell size and to neglect cell proliferation. Quantitative descriptions of morphogenetic processes will certainly require model refinements in these directions. While this seems feasible

for future investigations, the largest obstacle to overcome to enable simulations of interesting morphogenetic evolutions, such as the gastrulation process considered in [95], are limitations of the numerics. The computational effort to resolve the geometric properties in the required accuracy to obtain stable numerical schemes is huge [96–99]. Improvements in numerical analysis are certainly needed to reach comparable problem sizes. On the other side, the proposed model is one step towards more quantitative descriptions and asks for dedicated experiments with a moderate number of cells and within a controlled environment to parameterize and validate the two-scale model.

A Appendix

A.1 Illustration for shape classification

Here we illustrate how the spherical harmonics can be used to reconstruct the original shape. Note that for a reconstruction the values q_l^m need to be used, as we lose information going from q_l^m to q_l . Furthermore we use here values of q_l^m which are not normalized to obtain the same scale as in the original picture. As can be seen in Figure 17 the approximation already reproduces the original shape qualitatively with $l_{max} = 4$. Higher l_{max} improve only small details of the overall shape and for $l_{max} = 12$ differences are no longer visible, which suggests $l_{max} = 12$ to be sufficient for our purpose.

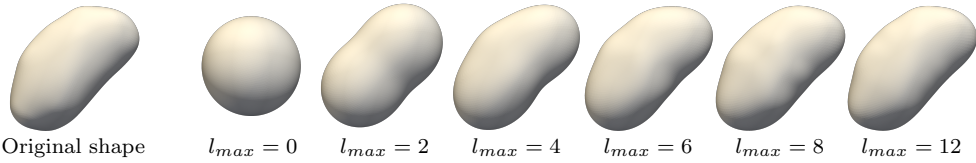


Fig. 17 Visualization of the shape classification with spherical harmonics. On the left the original shape is shown, on the right we show reconstructions of the shape $\sum_{l=0}^{l_{max}} \sum_{m=-l}^{m=l} q_l^m Y_l^m(\theta, \varphi)$ for different values l_{max} . With higher l_{max} the reconstructed shape resembles the original shape more and more.

A.2 Simulation details

In all simulations we use an adaptive grid whereby we always have at least seven grid points in the diffused interface of each cell. For simulations with 12 and 32 cells 50 time units are regarded. For the simulations with 92 cells 100 time units are regarded. There the first 10 time units are excluded from all evaluations to ensure that the system had enough time to deviate from the initial state. The parameters used in all simulations can be found in Table 1. For the simulations with 92 cells we consider $v_0 \in [0.1, 0.2, 0.3, 0.4]$.

Due to the diffuse interfaces of the phase-field approach a packing fraction of 100% is not feasible. Therefore in all simulations a packing fraction of 94% is used. This also resembles biological tissues as the importance of unoccupied spaces between cells was shown for example in [19].

Parameter	Explanation	Value
ϵ	width of the diffuse interface in the phase-field description	0.01
Ca	capillary number	10.0
In	interaction number	0.05
a_{rep}	strength of repulsive interaction	0.0625
a_{att}	strength of attractive interaction	0.48
τ_n	time step	0.005
D_r	rotational diffusion parameter	0.005
k_{fac}	range of the cell dependent bending stiffness	0.022
k_{lower}	minimum of the cell dependent bending stiffness	0.008

Table 1 Parameters used in all simulations

A.3 Calculation of irreducible surface Minkowski tensors

For the calculation of μ_p we use the zero-levelset of the cells as the cell contour. The zero-levelset was extracted with the help of *dune-tpmc* [100]. As this algorithm is based on a marching cubes algorithm the contours sometimes contain grid cell shaped artifacts. To get rid of these the cell contours were smoothed by replacing every coordinate with the mean of seven coordinates. The calculation of μ_p is done as described in [81] and the implementation follows closely the one in [101].

Acknowledgments

We acknowledge support by Maik Porrmann on the realization of the classical Canham/Helfrich problem and fruitful discussion with Simon Praetorius and Florian Roß on the implementation in AMDiS. This work was supported by the German Research Foundation (DFG) through the research unit FOR3013, “Vector- and Tensor-Valued Surface PDEs,” within project TP01, “Numerical methods for surface fluids” (project numbers VO 899/28-2) and TP05, “Ordering and defects on deformable surfaces” (project number VO 899/30-1). We further acknowledge computing resources at JSC under grant ”MORPH” and at ZIH under grant WIR.

References

- [1] Thompson, D.W.: On Growth and Form. Cambridge University Press, Cambridge (1917)
- [2] Heisenberg, C.-P., Bellaïche, Y.: Forces in tissue morphogenesis and patterning. *Cell* **153**, 948–962 (2013)
- [3] Salbreux, G., Charras, G., Paluch, E.: Actin cortex mechanics and cellular morphogenesis. *Trends in Cell Biology* **22**, 536–545 (2012)
- [4] Da Rocha, H.B., Bleyer, J., Turlier, H.: A viscous active shell theory of the cell cortex. *Journal of the Mechanics and Physics of Solids* **164**, 104876 (2022)

- [5] De Belly, H., Yan, S., Rocha, H.B., Ichbiah, S., Town, J.P., Zager, P.J., Estrada, D.C., Meyer, K., Turlier, H., Bustamante, C., Weiner, O.D.: Cell protrusions and contractions generate long-range membrane tension propagation. *Cell* **186**, 3049–3061 (2023)
- [6] Khoromskaia, D., Salbreux, G.: Active morphogenesis of patterned epithelial shells. *eLife* **12**, 75878 (2023)
- [7] Jülicher, F., Grill, S.W., Salbreux, G.: Hydrodynamic theory of active matter. *Reports on Progress in Physics* **81**, 076601 (2018)
- [8] Morris, R.G., Rao, M.: Active morphogenesis of epithelial monolayers. *Physical Review E* **100**, 022413 (2019)
- [9] Salbreux, G., Jülicher, F., Prost, J., Callan-Jones, A.: Theory of nematic and polar active fluid surfaces. *Physical Review Research* **4**, 033158 (2022)
- [10] Al-Izzi, S.C., Morris, R.G.: Morphodynamics of active nematic fluid surfaces. *Journal of Fluid Mechanics* **957**, 4 (2023)
- [11] Nitschke, I., Voigt, A.: Active nematodynamics on deformable surfaces. *Proceedings of the Royal Society A* **481**(2310), 20240380 (2025)
- [12] Torres-Sánchez, A., Millán, D., Arroyo, M.: Modelling fluid deformable surfaces with an emphasis on biological interfaces. *Journal of Fluid Mechanics* **872**, 218–271 (2019)
- [13] Reuther, S., Nitschke, I., Voigt, A.: A numerical approach for fluid deformable surfaces. *Journal of Fluid Mechanics* **900**, 8 (2020)
- [14] Krause, V., Voigt, A.: A numerical approach for fluid deformable surfaces with conserved enclosed volume. *Journal of Computational Physics* **486**, 112097 (2023)
- [15] Pormann, M., Voigt, A.: Shape evolution of fluid deformable surfaces under active geometric forces. *Physics of Fluids* **36**, 102120 (2024)
- [16] Nitschke, I., Voigt, A.: Beris-Edwards models on evolving surfaces: A Lagrange-D’Alembert approach. *Advances in Differential Equations* **30**, 335–420 (2025)
- [17] Torres-Sánchez, A., Santos-Oliván, D., Arroyo, M.: Approximation of tensor fields on surfaces of arbitrary topology based on local Monge parametrizations. *Journal of Computational Physics* **405**, 109168 (2020)
- [18] Nestler, M., Nitschke, I., Voigt, A.: A finite element approach for vector- and tensor-valued surface PDEs. *Journal of Computational Physics* **389**, 48–61 (2019)

- [19] Kim, S., Pochitaloff, M., Stooke-Vaughan, G.A., Campàs, O.: Embryonic tissues as active foams. *Nature Physics* **17**, 859–866 (2021)
- [20] Fuhrmann, J.F., Krishna, A., Paijmans, J., Duclut, C., Cwikla, G., Eaton, S., Popović, M., Jülicher, F., Modes, C.D., Dye, N.A.: Active shape programming drives drosophila wing disc eversion. *Science Advances* **10**, 0860 (2024)
- [21] Runser, S., Vetter, R., Iber, D.: SimuCell3D: three-dimensional simulation of tissue mechanics with cell polarization. *Nature Computational Science* **4**, 299–309 (2024)
- [22] Ouzeri, A., Kale, S., Chahare, N., Torres-Sanchez, A., Santos-Olivan, D., Trepát, X., Arroyo, M.: Theory of multiscale epithelial mechanics under stretch: from active gels to vertex models. *bioRxiv* (2025) <https://doi.org/10.1101/2025.03.23.644792>
- [23] Seung, H.S., Nelson, D.R.: Defects in flexible membranes with crystalline order. *Physical Review A* **38**, 1005–1018 (1988)
- [24] Lehtinen, O., Kurasch, S., Krashennnikov, A., Kaiser, U.: Atomic scale study of the life cycle of a dislocation in graphene from birth to annihilation. *Nature Communications* **4**(1), 2098 (2013)
- [25] Benoit–Maréchal, L., Nitschke, I., Voigt, A., Salvalaglio, M.: Mesoscale modeling of deformations and defects in thin crystalline sheets. *Mechanics of Materials* **198**, 105114 (2024)
- [26] Saw, T.B., Doostmohammadi, A., Nier, V., Kocgozlu, L., Thampi, S., Toyama, Y., Marcq, P., Lim, C.T., Yeomans, J.M., Ladoux, B.: Topological defects in epithelia govern cell death and extrusion. *Nature* **544**, 212–216 (2017)
- [27] Nitschke, I., Reuther, S., Voigt, A.: Liquid crystals on deformable surfaces. *Proceedings of the Royal Society A* **476**, 20200313 (2020)
- [28] Guillamat, P., Blanch-Mercader, C., Pernollet, G., Kruse, K., Roux, A.: Integer topological defects organize stresses driving tissue morphogenesis. *Nature Materials* **21**, 588–597 (2022)
- [29] Hoffmann, L.A., Carenza, L.N., Eckert, J., Giomi, L.: Theory of defect-mediated morphogenesis. *Science Advances* **8**, 2712 (2022)
- [30] Maroudas-Sacks, Y., Garion, L., Shani-Zerbib, L., Livshits, A., Braun, E., Keren, K.: Topological defects in the nematic order of actin fibres as organization centres of hydra morphogenesis. *Nature Physics* **17**, 251–259 (2021)
- [31] Maroudas-Sacks, Y., Suganthan, S., Garion, L., Ascoli-Abbina, Y., Westfried, A., Dori, N., Pasvinter, I., Popović, M., Keren, K.: Mechanical strain focusing at

- topological defect sites in regenerating hydra. *Development* **152**, 204514 (2025)
- [32] Bi, D., Yang, X., Marchetti, M.C., Manning, M.L.: Motility-driven glass and jamming transitions in biological tissues. *Physical Review X* **6**, 021011 (2016)
- [33] Camley, B.A., Zhang, Y., Zhao, Y., Li, B., Ben-Jacob, E., Levine, H., Rappel, W.-J.: Polarity mechanisms such as contact inhibition of locomotion regulate persistent rotational motion of mammalian cells on micropatterns. *Proceedings of the National Academy of Science (USA)* **111**, 14770–14775 (2014)
- [34] Mueller, R., Yeomans, J.M., Doostmohammadi, A.: Emergence of active nematic behavior in monolayers of isotropic cells. *Physical Review Letters* **122**, 048004 (2019)
- [35] Loewe, B., Chiang, M., Marenduzzo, D., Marchetti, M.C.: Solid-liquid transition of deformable and overlapping active particles. *Physical Review Letters* **125**, 038003 (2020)
- [36] Wenzel, D., Voigt, A.: Multiphase field models for collective cell migration. *Physical Review E* **184**, 054410 (2021)
- [37] Farhadifar, R., Roper, J.-C., Algouy, B., Eaton, S., Jülicher, F.: The influence of cell mechanics, cell-cell interactions, and proliferation on epithelial packing. *Current Biology* **17**, 2095–2104 (2007)
- [38] Rozman, J., Chaithanya, K., Yeomans, J.M., Sknepnek, R.: Vertex model with internal dissipation enables sustained flows. *Nature Communications* **16**, 530 (2025)
- [39] Happel, L., Wenzel, D., Voigt, A.: Effects of curvature on epithelial tissue - coordinated rotational movement and other spatiotemporal arrangements. *EPL* **138**, 67002 (2022)
- [40] Happel, L., Voigt, A.: Coordinated motion of epithelial layers on curved surfaces. *Physical Review Letters* **132**, 078401 (2024)
- [41] Canham, P.B.: The minimum energy of bending as a possible explanation of the biconcave shape of the human red blood cell. *Journal of Theoretical Biology* **26**, 61 (1970)
- [42] Helfrich, W.: Elastic properties of lipid bilayers: Theory and possible experiments. *Zeitschrift für Naturforschung C* **28**, 693–703 (1973)
- [43] Arroyo, M., DeSimone, A.: Relaxation dynamics of fluid membranes. *Physical Review E* **79**, 031915 (2009)
- [44] Reuther, S., Voigt, A.: The interplay of curvature and vortices in flow on curved surfaces. *Multiscale Modeling & Simulation* **13**, 632–643 (2015)

- [45] Reuther, S., Voigt, A.: Erratum: The interplay of curvature and vortices in flow on curved surfaces. *Multiscale Modeling & Simulation* **16**, 1448–1453 (2018)
- [46] Grossman, D., Joanny, J.-F.: Instabilities and geometry of growing tissues. *Physical Review Letters* **129**, 048102 (2022)
- [47] Claussen, N.H., Brauns, F.: Mean-field model for active plastic flow of epithelial tissue. *PRX Life* **3**(2), 023002 (2025)
- [48] Armengol-Collado, J.-M., Livio, N.C., Giomi, L.: Hydrodynamics and multiscale order in confluent epithelia. *eLife* **13** (2024)
- [49] Nejad, M.R., Yeomans, J.M.: Coarse-graining dense, deformable active particles. *arXiv:2501.07280* (2025)
- [50] Monfared, S., Ardaševa, A., Doostmohammadi, A.: Multi-phase-field models of biological tissues. *arXiv:2503.05053* (2025)
- [51] Jain, H.P., Voigt, A., Angheluta, L.: Robust statistical properties of T1 transitions in a multi-phase field model of cell monolayers. *Scientific Reports* **13**, 10096 (2023)
- [52] Bachini, E., Krause, V., Nitschke, I., Voigt, A.: Derivation and simulation of a two-phase fluid deformable surface model. *Journal of Fluid Mechanics* **977**, 41 (2023)
- [53] Krause, V., Voigt, A.: Wrinkling of fluid deformable surfaces. *Journal of The Royal Society Interface* **21**, 20240056 (2024)
- [54] Salvalaglio, M., Voigt, A., Wise, S.M.: Doubly degenerate diffuse interface models of surface diffusion. *Mathematical Methods in Applied Science* **44**, 5385–5405 (2021)
- [55] Gu, R., Wang, X., Gunzburger, M.: Simulating vesicle-substrate adhesion using two phase field functions. *Journal of Computational Physics* **275**, 626–641 (2014)
- [56] Marth, W., Voigt, A.: Collective migration under hydrodynamic interactions: a computational approach. *Interface Focus* **6**, 20160037 (2016)
- [57] Wenzel, D., Praetorius, S., Voigt, A.: Topological and geometrical quantities in active cellular structures. *Journal of Chemical Physics* **150**, 164108 (2019)
- [58] Dziuk, G., Elliott, C.M.: Finite element methods for surface PDEs. *Acta Numerica* **22**, 289–396 (2013)
- [59] Nitschke, I., Voigt, A.: Observer-invariant time derivatives on moving surfaces. *Journal of Geometry and Physics* **173**, 104428 (2022)

- [60] Caetano, D., Elliott, C.M., Grasselli, M., Poiatti, A.: Regularization and separation for evolving surface Cahn–Hilliard equations. *SIAM Journal on Mathematical Analysis* **55**, 6625–6675 (2023)
- [61] Sischka, J.M., Voigt, A.: Two-phase fluid deformable surfaces with constant enclosed volume and phase-dependent bending and gaussian rigidity. *Computer Methods in Applied Mechanics and Engineering* **to appear** (2025)
- [62] Jain, H.P., Voigt, A., Angheluta, L.: From cell intercalation to flow, the importance of T1 transitions. *Physical Review Research* **6**, 033176 (2024)
- [63] Monfared, S., Ravichandran, G., Andrade, J., Doostmohammadi, A.: Mechanical basis and topological routes to cell elimination. *eLife* **12**, 82435 (2023)
- [64] Aland, S., Rätz, A., Röger, M., Voigt, A.: Buckling instability of viral capsids—a continuum approach. *Multiscale Modeling & Simulation* **10**, 82–110 (2012)
- [65] Barrett, J.W., Garcke, H., Nürnberg, R.: On the parametric finite element approximation of evolving hypersurfaces in \mathbb{R}^3 . *Journal of Computational Physics* **227**, 4281–4307 (2008)
- [66] Praetorius, S., Stenger, F.: Dune-CurvedGrid - A Dune module for surface parametrization. *Archive of Numerical Software* **6**, 1–27 (2022)
- [67] Praetorius, S., Voigt, A.: Collective cell behavior - a cell-based parallelization approach for a phase field active polar gel model. In: Binder, K., Müller, M., Trautmann, A. (eds.) *NIC Symposium 2018*, vol. 49, pp. 369–376. Forschungszentrum Jülich GmbH, Zentralbibliothek, Jülich (2018)
- [68] Adaptive Multi-Dimensional Simulations. <https://gitlab.com/amdis/amdis>
- [69] Vey, S., Voigt, A.: AMDiS: Adaptive multidimensional simulations. *Computation and Visualization in Science* **10**, 57–67 (2007)
- [70] Witkowski, T., Ling, S., Praetorius, S., Voigt, A.: Software concepts and numerical algorithms for a scalable adaptive parallel finite element method. *Advances in Computational Mathematics* **41**, 1145–1177 (2015)
- [71] Bastian, P., Blatt, M., Dedner, A., Dreier, N.-A., Engwer, C., Fritze, R., Gräser, C., Grüninger, C., Kempf, D., Klöfkorn, R., Ohlberger, M., Sander, O.: The Dune framework: Basic concepts and recent developments. *Computers & Mathematics with Applications* **81**, 75–112 (2021)
- [72] Sander, O.: *DUNE — The Distributed and Unified Numerics Environment*. Springer, Berlin (2020)
- [73] Alkämper, M., Dedner, A., Klöfkorn, R., Nolte, M.: The dune-alugrid module. *Archive of Numerical Software* **4**, 1–28 (2016)

- [74] Seifert, U.: Configurations of fluid membranes and vesicles. *Advances in Physics* **46**, 13–137 (1997)
- [75] Thomson, J.J.: On the structure of the atom: an investigation of the stability and periods of oscillation of a number of corpuscles arranged at equal intervals around the circumference of a circle; with application of the results to the theory of atomic structure. *The London, Edinburgh, and Dublin Philosophical Magazine and Journal of Science* **7**, 237–265 (1904)
- [76] Tarnai, T., Gáspár, Z.: Multi-symmetric close packings of equal spheres on the spherical surface. *Acta Crystallographica Section A* **43**, 612–616 (1987)
- [77] Backofen, R., Voigt, A., Witkowski, T.: Particles on curved surfaces: A dynamic approach by a phase-field-crystal model. *Physical Review E* **81**, 025701 (2010)
- [78] Backofen, R., Gräf, M., Potts, D., Praetorius, S., Voigt, A., Witkowski, T.: A continuous approach to discrete ordering on \mathbb{S}^2 . *Multiscale Modeling & Simulation* **9**, 314–334 (2011)
- [79] Olshanskii, M.: On equilibrium states of fluid membranes. *Physics of Fluids* **35**, 062111 (2023)
- [80] Nestler, M., Voigt, A.: Stability of rotating equilibrium states of fluid deformable surfaces. *Proceedings of Applied Mathematics and Mechanics* **2023**, 202300044 (2023)
- [81] Happel, L., Hardering, H., Praetorius, S., Voigt, A.: Surface Minkowski tensors to characterize shapes on curved surfaces. *arXiv:2506.13880* (2025)
- [82] Schröder-Turk, G.E., Mickel, W., Kapfer, S.C., Klatt, M.A., Schaller, F.M., Hoffmann, M.J.F., Kleppmann, N., Armstrong, P., Inayat, A., Hug, D., Reichelsdorfer, M., Peukert, W., Schwieger, W., Mecke, K.: Minkowski tensor shape analysis of cellular, granular and porous structures. *Advanced Materials* **23**, 2535–2553 (2011)
- [83] Wei, D., Zhao, B., Gan, Y.: Surface reconstruction with spherical harmonics and its application for single particle crushing simulations. *Journal of Rock Mechanics and Geotechnical Engineering* **14**, 232–239 (2022)
- [84] Zhou, B., Wang, J.: Generation of a realistic 3D sand assembly using X-ray micro-computed tomography and spherical harmonic-based principal component analysis. *International Journal for Numerical and Analytical Methods in Geomechanics* **41**, 93–109 (2017)
- [85] Kazhdan, M., Funkhouser, T., Rusinkiewicz, S.: Rotation invariant spherical harmonic representation of 3D shape descriptors. In: *Proceedings of the 2003 Eurographics/ACM SIGGRAPH Symposium on Geometry Processing. SGP '03*,

pp. 156–164. Eurographics Association, Goslar, Germany (2003)

- [86] Zhou, B., Wang, J., Zhao, B.: Micromorphology characterization and reconstruction of sand particles using micro x-ray tomography and spherical harmonics. *Engineering Geology* **184**, 126–137 (2015)
- [87] Horn, B.K.P., Hilden, H.M., Negahdaripour, S.: Closed-form solution of absolute orientation using orthonormal matrices. *Journal of Optical Society of America A* **5**, 1127–1135 (1988)
- [88] Al-Izzi, S.C., Alexander, G.P.: Chiral active membranes: Odd mechanics, spontaneous flows, and shape instabilities. *Physical Review Research* **5**, 043227 (2023)
- [89] Tanner, K., Mori, H., Mroue, R., Bruni-Cardoso, A., Bissell, M.J.: Coherent angular motion in the establishment of multicellular architecture of glandular tissues. *Proceedings of the National Academy of Science (USA)* **109**, 1973–1978 (2012)
- [90] Wang, H., Lacoche, S., Huang, L., Xue, B., Muthuswamy, S.K.: Rotational motion during three-dimensional morphogenesis of mammary epithelial acini relates to laminin matrix assembly. *Proceedings of the National Academy of Science (USA)* **110**, 163–168 (2013)
- [91] Baumgart, T., Hess, S., Webb, W.: Imaging coexisting fluid domains in biomembrane models coupling curvature and line tension. *Nature* **425**, 821–824 (2003)
- [92] Elliott, C.M., Stinner, B.: Computation of two-phase biomembranes with phase dependent material parameters using surface finite elements. *Communications in Computational Physics* **13**, 325–360 (2013)
- [93] Barrett, J.W., Garcke, H., Nürnberg, R.: Finite element approximation for the dynamics of fluidic two-phase biomembranes. *ESAIM: Mathematical Modelling and Numerical Analysis* **51**, 2319–2366 (2017)
- [94] Bell, S., Lin, S.-Z., Rupprecht, J.-F., Prost, J.: Active nematic flows over curved surfaces. *Physical Review Letters* **129**, 118001 (2022)
- [95] Münster, S., Jain, A., Mietke, A., Pavlopoulos, A., Grill, S.W., Tomancak, P.: Attachment of the blastoderm to the vitelline envelope affects gastrulation of insects. *Nature* **568**, 395–399 (2019)
- [96] Hardering, H., Praetorius, S.: Tangential errors of tensor surface finite elements. *IMA Journal of Numerical Analysis* **43**, 1543–1585 (2023)
- [97] Bachini, E., Brandner, P., Jankuhn, T., Nestler, M., Praetorius, S., Reusken, A.,

- Voigt, A.: Diffusion of tangential tensor fields: numerical issues and influence of geometric properties. *Journal of Numerical Mathematics* **32**(1), 55–75 (2024)
- [98] Sass, H., Reusken, A.: An accurate and robust eulerian finite element method for partial differential equations on evolving surfaces. *Computers & Mathematics with Applications* **146**, 253–270 (2023)
- [99] Elliott, C.M., Sales, T.: A fully discrete evolving surface finite element method for the cahn–hilliard equation with a regular potential. *Numerische Mathematik* **157**, 663–715 (2025)
- [100] Engwer, C., Nüßing, A.: Geometric reconstruction of implicitly defined surfaces and domains with topological guarantees. *ACM Transactions of Mathematical Software* **44** (2018)
- [101] Praetorius, S.: SurfaceMinkowski.jl: a Julia package for computing surface Minkowski functionals. <https://gitlab.mn.tu-dresden.de/spraetor/SurfaceMinkowski.jl>